Classical and Quantum Gravity

PURPOSE-LED PUBLISHING™

ACCEPTED MANUSCRIPT

Frequency domain thermoelastic optimization strategy for the TianQin inertial sensor support

To cite this article before publication: Fulong Wei *et al* 2026 *Class. Quantum Grav.* in press https://doi.org/10.1088/1361-6382/ae5f57

Frequency domain thermoelastic optimization strategy for the TianQin inertial sensor support

Fulong Wei[1], Jinlong Ma[2], Shaobo Qu[1], Xingyu Yan[1], Shen Zhan[1], Xiaobing Luo[2*] and Zebing Zhou[1*]

(1. National Gravitation Laboratory, MOE Key Laboratory of Fundamental Physical Quantities Measurements, and School of Physics, Huazhong University of Science and Technology, Wuhan 430074, People's Republic of China;
2. School of Energy and Power Engineering, Huazhong University of Science and Technology, Wuhan 430074, People's Republic of China)

*Corresponding author email: luoxb@hust.edu.cn; zhouzb@hust.edu.cn

Abstract: Thermoelastic stability is a critical requirement for inertial sensors in the space-based gravitational wave detection, with the relative distance stability between the inertial sensor and the optical bench being a key performance driver. In existing studies, systematic optimization strategy for the thermoelastic compensation support of the inertial sensor has yet to be developed. In this study, a unified design framework integrating parametric geometric modeling, thermoelastic simulation, and the optimization algorithms is established and applied to the optimization of a typical inertial sensor support structure. A set of practical design strategy is proposed: (i) steady temperature and heat sources have negligible coupling effects into the frequency-domain thermoelastic analysis; (ii) the level of the thermal noise should be treated as a constraint in the optimization design; (iii) the lowest frequency within the target frequency band may be selected as the representative for the full band. Following these strategy, the gain for the thermoelastic displacement reduces from 3.28×10^{-8} m/W@ 0.1 mHz to 5.81×10^{-9} m/W@ 0.1 mHz for an improved configuration. The gain for the temperature fluctuation reaches 0.94×10^{-4} K/W@ 0.1 mHz, which remains within the acceptable limits. This work provides systematic optimization methodology and design criteria for the future space inertial sensors.

Keywords: Gravititional wave detection; Space inertial sensor; Thermoelastic analysis; Thermal optimization

Nomenclature

ρ	Density	kg/m^3	θ	Complex temperature	K

c	Specific heat capacity	kJ/(kg·K)	$\dot{Q}$	Complex self-generating heat	W/m^3
k	Thermal conductivity	W/(m·K)	$\underline{\varepsilon}$	Complex strain tensor	/
ω	Angular frequency	rad·s^{-1}	$\tilde{N}$	Spatial gradient operator	m^{-1}
Q	Self-generating heat	W/m^3	$\underline{\varepsilon}_{th}$	Complex thermal strain tensor	/
Q_0	Steady self-generating heat	W/m^3	I	Second-order identity tensor	/
t	Time	s	$\dot{\mathbf{u}}$	Complex displacement amplitude	m
T	Temperature	K	$\underline{\sigma}$	Complex stress tensor	Pa
T_0	Steady temperature	K	$\tilde{\mathbf{F}}$	Complex body-force density	N·m^{-3}
α	Coefficient of thermal expansion	K^{-1}	$S_A^{1/2}$	Amplitude spectral density for A	A/Hz$^{1/2}$

1. Introduction

Space-based gravitational wave detection represents a new frontier in the development of the future space science, enabling the acquisition of abundant mid to low-frequency gravitational wave signals to deeply explore the evolution of the universe [1-3]. For example, the TianQin mission, one of the Chinese pioneering space-based gravitational wave detection projects, is designed to observe gravitational waves (GWs) in the frequency range of 0.1 mHz to 1 Hz [4]. To achieve high-precision detection, the TianQin mission requires that the residual acceleration noise does not exceed 1 fm/s^2/Hz$^{1/2}$, and that the test-mass-to-test-mass (TM-to-TM) displacement measurement noise remains below 1 pm/Hz$^{1/2}$ [5]. Among the various noise sources in TianQin, temperature fluctuations (TFs) are a significant contributor [6], potentially affecting the measurements through direct forces such as the radiation pressure, radiometer, and the outgassing effects [7].

In addition to directly exerting forces on the TM, temperature can also indirectly interfere within the laser interferometry system. According to the studies from the European space-based GW detector LISA, these effects are mainly manifested as thermally induced strains in the opto-mechanical system and variations in the refractive index [8]. Unlike the effect of the temperature

on the refractive index, which occurs only on the optical components, thermoelastic effects are widely present within the structural framework of the core payloads inside the GW detectors [9]. The prevailing view suggests that the thermal effects can induce extra strains, thereby compromising the structural stability of the payloads and introducing potential noise sources [10]. The TianQin mission alternates between non-science and science modes, the latter being the core phase for gravitational wave detection. Thermo-elastic effects during these phases include a transient offset and frequency-dependent thermoelastic deformation (TED). During the non-science mode, variations in spacecraft temperature may induce transient TED. Before science mode, the spacecraft's temperature and resulting transient TED are monitored by the thermal diagnostic system[31], while the interferometer is adjusted to compensate for transient effects. However, the frequency domain (FD) TED fluctuation is associated with the periodic temperature variations during the scientific mode. Therefore the FD TED fluctuation becomes the primary concern for the in-orbit observations compared with the transient offset. This study focuses on the FD characteristics of the TED fluctuation.

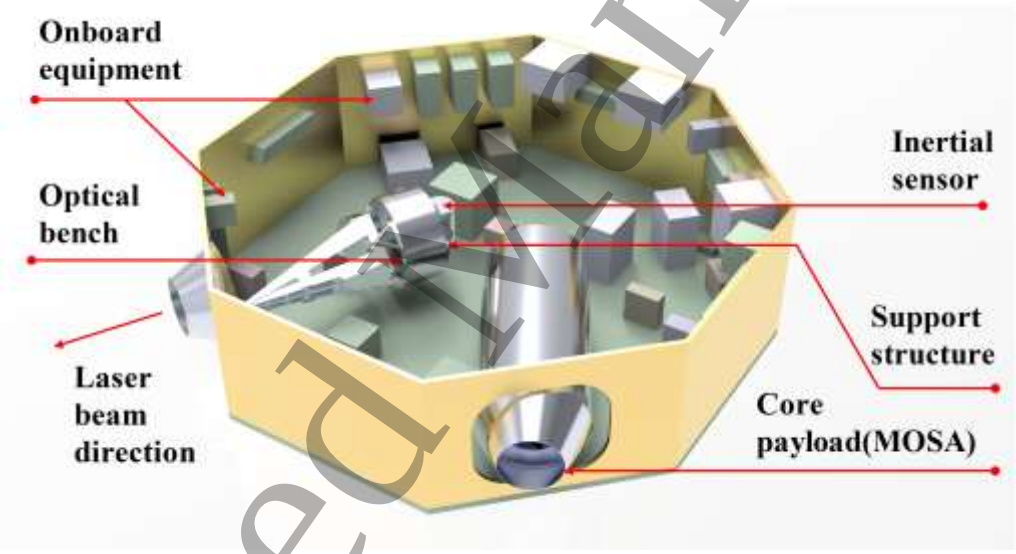

Figure 1. Illustration of the structure of the TianQin SC.

Fig. 1 presents a schematic diagram of the TianQin spacecraft (SC) structure. In the SC, the core payload module, referred to as the Moving Optical Sub-Assembly (MOSA), is the most critical scientific measurement instrument [11]. The three primary optical components—the telescope, the optical bench (OB), and the inertial sensor (IS)—are installed on the inertial sensor support structure (ISS) inside MOSA [12]. The ISS serves as the mechanical interface connecting these optical instruments and linking them to the spacecraft through a pivot point. Consequently, the ISS plays a critical role in preserving the relative alignment of these components throughout integration, testing, and in-orbit operation. Improving the thermoelastic stability of the ISS is therefore essential, with particular emphasis on improving the relative distance stability between the OB and the IS along the laser beam direction.

Several approaches can be adopted to improve the thermal stability, one of which is to utilize ultra-low thermal deformation materials to reduce TED. This approach enables the achievement of the thermal stability while allowing for simpler structural configurations by directly lowering the effective coefficient of the thermal expansion (CTE). Materials such as single-crystal silicon and microcrystalline glass exhibit extremely low CTEs [13]. However, their zero-expansion temperature points are typically located at ultral low temperature environments and therefore failing to meet the operational temperature requirements of the GW detectors. Carbon Fiber Reinforced Polymer (CFRP) exhibits an extremely low CTE [14,15], as low as 10^{-6} K^{-1}. Nevertheless, its outgassing characteristics may introduce potential adverse effects in the highly sensitive vacuum environment of MOSA and therefore require careful evaluation [16]. Glass-ceramic materials such as Zerodur offer excellent thermoelastic stability, with CTE as low as 10^{-8} K^{-1}. However, their inherent brittleness, fabrication complexity, and limited stability under launch environments substantially restrict their practical deployment for the ISS [17]. Invar alloys represent another type of low CTE materials. Their CTE can be reduced to below 10^{-6} K^{-1}. The mass of SC components is increased due to their high density, and undesirable interference with ISs and other sensitive electronic devices may be introduced by their magnetic properties [18].

Another major approach to mitigate thermoelastic effects is through the innovative structural design. A truss-type structural design is adopted, in which TED are redirected into degrees of freedom that have minimal impact on the system performance through an appropriate geometric layout and constraint configuration [19]. In addition, the flexible structural designs are often employed for the optical components that undergo significant thermal expansion to accommodate the thermal strain and stress. This method is better suited for the compensation of the large static offset induced by the temperature variations [20]. Finally, a widely used solution is the thermoelastic compensation structure (TECS) [21]. The core strategy is to exploit the difference in CTEs among two or more materials. By coupling these materials through welding, bonding, or other joining techniques, the individual components expand in the different directions when heated, such that their TEDs compensate for each other. As a result, the net TED can be significantly reduced, and in some cases brought close to zero.

LISA has investigated the application of TECSs in the GW detection. In the ground-based simulation experiments of the opto-mechanical system performance, Invar alloy is employed as the structural support, while aluminum alloy is used as the TECS [22]. The experimental results demonstrate that the structural deformation noise can be effectively suppressed from 60 $pm/Hz^{1/2}$ to 1.5 $pm/Hz^{1/2}$ within the specified operational bandwidth. In addition, LISA investigated the thermoelastic behavior of the ISS and derived a corresponding design methodology based on a one-dimensional model for the on-orbit operational conditions [23].

Similarly, other researchers employ simplified models instead of the actual structures and designed a structure for the space telescope [24]. Taiji team investigated a TECS consisting of a hollow titanium alloy tube as the primary support and an aluminum alloy tube as the compensation stage. Using an isothermal thermal expansion model in the time domain, the effective CTE of the compensation structure is both predicted and experimentally measured [25]. The main issues of current studies can be summarized as follows. Most existing studies remain at the conceptual design stage, and the use of one-dimensional models provides insufficient accuracy for the analysis of more complex TECSs for ISS. Moreover, there is a lack of comprehensive understanding of the FD thermodynamic behavior in the GW detection, as well as a lack of corresponding optimization-oriented design considerations.

This paper presents a method to improve the TED stability of the TECS through thermal optimization techniques. A typical ISS was optimized using the co-simulation approach integrating parametric geometric modeling, thermoelastic simulation, and optimization algorithms. The thermoelastic optimization strategy of the ISS were proposed. Multiple optimization algorithms were employed, and the thermal and thermoelastic performance of the system were assessed and compared before and after optimization. Finally, a preliminary ISS designed specifically for the TianQin project was developed. The methodology proposed can be broadly applied to the design of mechanical systems in other gravitational wave detection missions.

2. Model

2.1 Thermoelastic coupled analysis

In a GW detector, the IS and the OB are mounted in a face-to-face configuration. Fig. 2 (a) presents a schematic diagram of the mounting relationship between the IS and the OB without compensation. The optical window of the IS is directly parallel to the OB in the x-axis direction. The ISS acts as an intermediate medium in the heat transfer path, receiving the potential heat from the OB while simultaneously exerting a direct thermal influence on the IS through the supporting interface. Fig. 2 (b) shows a compensated IS mounting structure. Titanium alloy and aluminum alloy are considered for the supporting and compensation stages, respectively. As commonly used materials, both materials offer advantages in terms of the structural support strength and non-magnetic behavior. The end of the supporting stage is connected to the compensation stage through the friction welding. The compensation stage and the IS are connected via a screw-fastened mechanical interface. Table 1 lists the thermal and mechanical properties of the components [26]. Particularly, the thermal diffusivity of the Al alloy is 6.58×10^{-5} m^2/s, while that of the Ti alloy is 2.70×10^{-6} m^2/s. The CTE of the Al alloy is roughly three times higher than the Ti alloy.

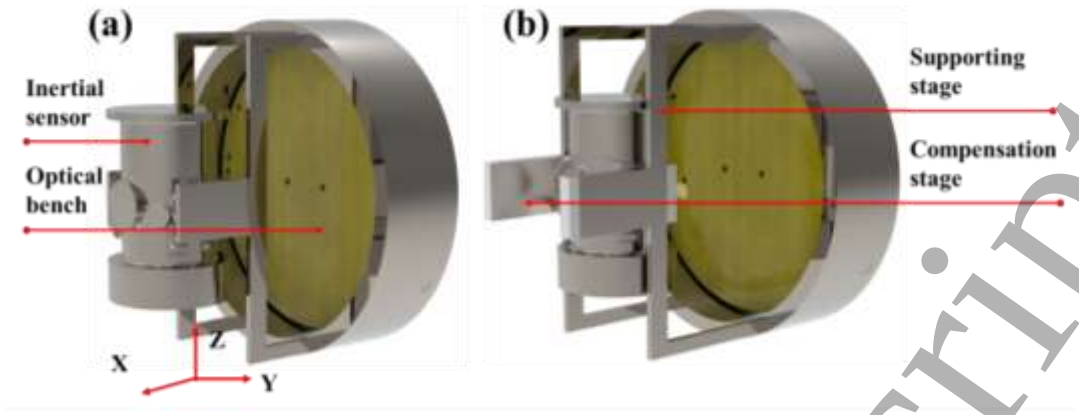

Figure 2. Structure diagram of the support structure for the IS and OB: (a) before compensation; (b) after compensation.

Table 1. Thermal and mechanical properties of the components.

Name	Material	Thermal conductivity ($W \cdot m^{-1} \cdot K^{-1}$)	Density ($kg \cdot m^{-3}$)	Specific heat capacity ($J \cdot kg^{-1} \cdot K^{-1}$)	Coefficient of thermal expansion (K^{-1})	Young's modulus (GPa)	Poisson's ratio
Supporting stage	Ti alloy	7.5	4940	710	8.6×10^{-6}	70	0.33
Compensation stage	Al alloy	238	2700	900	2.4×10^{-5}	105	0.32

As stated above, the thermal performance analysis of the ISS focuses on the FD characteristics of the temperature and the TED fluctuations. The FD finite element (FE) method is employed for simulation to determine the thermal characteristics under the current design. The following assumptions are made based on the thermal environment surrounding the ISS, respectively:

(a) With the IS maintained under an ultra-stable thermal environment, temperature variations are small, and the temperature dependence of the material's thermal properties can be neglected [27];

(b) Thermal loads are directly included in the elasticity equations, ignoring any influence of the thermal stress on the temperature field. Thus, the temperature distribution is governed mainly by the external heat sources, without considering stress-induced feedback heating;

Under the periodic sinusoidal heat load at a given frequency, the temperature response can be assumed sinusoidal and periodic around the equilibrium temperature. The time-dependent problem can be replaced by an equivalent linear steady-state problem in the FD. The temperature decomposition described can be expressed as:

$$T(t) = T_0 + \tilde{T}e^{i\omega t} \quad (1)$$

The aforementioned temperature consists of both the steady-state temperature and the harmonic fluctuation. The frequency spectrum of the TFs can be represented as:

$$\tilde{T} = T_m e^{jwt} \tag{2}$$

Similarly, the volume heat source can be expressed as:

$$Q(t) = Q_0 + \tilde{Q} \tag{3}$$

The oscillatory component of the heat source can be represented as:

$$\tilde{Q} = Q_m e^{jwt} \tag{4}$$

By substituting Eqs. (1,3) into the heat conduction equation, Eqs. (5–6) are obtained:

$$\tilde{N} \times (-k\tilde{N}T(t)) + Q(t) = 0 \tag{5}$$

$$jwrC_pT_m e^{jwt} + \tilde{N} \times (-k\tilde{N}T_0) + \tilde{N} \times (-k\tilde{N}T_m)e^{jwt} + Q_0 + Q_m e^{jwt} = 0 \tag{6}$$

The static offset of the volume heat source directly affects the magnitude and spatial distribution of the steady-state temperature, satisfying the following steady-state heat conduction equation:

$$\tilde{N} \times (-k\tilde{N}T_0) + Q_0 = 0 \tag{7}$$

Since Eq. (6) is a linear differential equation, substituting Eq. (7) into it yields:

$$jwrC_p\tilde{T} + \tilde{N} \times (-k\tilde{N}\tilde{T}) + \tilde{Q} = 0 \tag{8}$$

Eq. (8) no longer contains the steady-state temperature or steady-state heat source terms, demonstrating that the steady volume heat source or steady temperature boundary conditions have no coupling effect on the temperature harmonic response in the FD. The thermal strain tensor also exhibits a harmonic form, and can be expressed as:

$$\tilde{\varepsilon}_{th} = a\tilde{T}\mathbf{I} \tag{9}$$

Eq. (9) indicates that the frequency of the thermal strain is strictly identical to that of the TF, indicating that no frequency coupling, harmonic generation, or mixing effects arise in the thermal strain response. The constitutive relationship between strain and stress can be expressed as:

$$\tilde{\sigma} = \mathbf{C} : (\tilde{\varepsilon} - \tilde{\varepsilon}_{th}) \tag{10}$$

The geometric relationship between the displacement tensor and the strain tensor can be expressed as:

$$\tilde{\varepsilon} = \frac{1}{2}(\tilde{N}\tilde{u} + (\tilde{N}\tilde{u})^T) \tag{11}$$

The strain of the elastic material under external loads is described by the momentum balance equation:

$$-w^2 r\tilde{u} + \tilde{N} \cdot \tilde{\sigma} = \tilde{F} \tag{12}$$

By solving the constitutive, geometric, and momentum equations in the FD, the harmonic response of the thermal strain can be obtained [30].

It is worth noting that some uncertainties remain in the model setup, particularly those associated with radiative effects in the multilayer insulation (MLI) and contact heat transfer. The surface of the support is covered with MLI, providing effective radiation shielding [28,29].

Therefore, the influence of radiation on the optimization results is expected to be tiny. In addition, the effects of friction welding and bolted interfaces remain to be evaluated in the optimization, and they are discussed in the following section.

Thermal noise surrounding the ISS is largely attributed to the variations in the solar heat flux. Moreover, the temperature asymmetry along the x-axis may arise from the telescope and the OB [27]. If the asymmetry originates from the noise associated with the telescope, a thermal diagnostics system [31] is typically required to monitor the temperature signals at the mounting interfaces in orbit, thereby prescribing TF boundary condition T. Correspondingly, if the asymmetry arises from the thermal source of the components on the OB, the heat source fluctuation boundary condition Q should be imposed. Hence, a thermal noise source H at a single frequency of 0.1 mHz and a fixed boundary condition is applied at the mounting interface in the simulation.

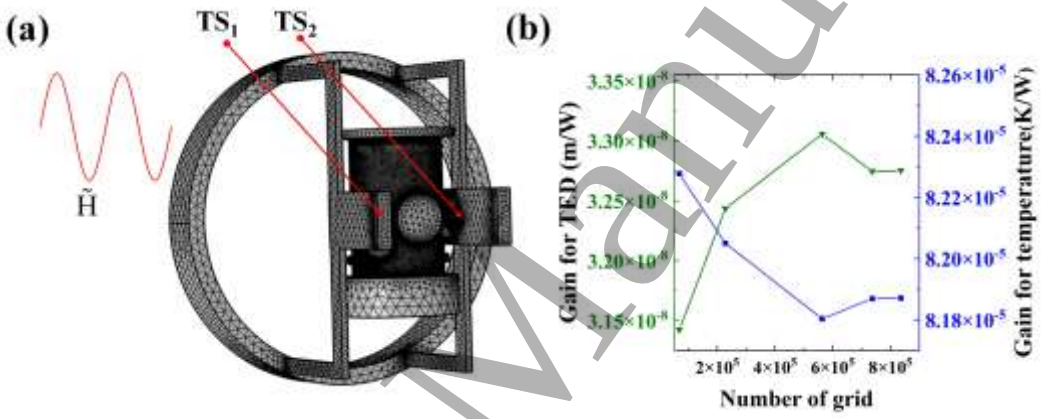

Figure 3. Grid independent validation: (a) mesh diagram; (b) gain for the transfer function varies with the grid number.

An unstructured mesh is employed for discretization, and the grid independence validation is performed as shown in Fig. 3. The temperature measurement points TS_1 and TS_2 are at the ends of the support stage and the compensation stage, respectively. The thermal and structural analyses are conducted independently for the conventional spacecraft thermal analysis approaches. It is necessary to examine whether refinements of the thermal model mesh, adjustments to the mapping procedure, or refinements of the structural FE model lead to any changes in the computed performance for the entire thermoelastic analysis chain [32]. Fortunately, the FE simulation software COMSOL employed in this study integrates both analyses within a fully coupled framework using a single FE mesh. Nonetheless, the mesh dependency checks for both the thermal and thermoelastic analyses are still required.

The gain for the temperature and the gain for TED are defined in Eq. (13-15) and validated. Fig. 3 (b) presents the results of the grid independence verification at the point TS_2. As the number of the mesh elements increases to approximately 7.37×10^5, variations in the gains

become negligible. Hence, a total of 737,357 mesh elements is chosen for the original model. During the optimization process, the mesh element number varies with the evolving geometry. To reduce the impact of such mesh variations on the results of the optimization, all the mesh parameters specified in Table 2 are maintained unchanged throughout the optimization process.

$$\left|Y_{TS1} - \text{[illegible]}\right| = \left|S_{TS_1}^{1/2}(f)/S_{\text{[illegible]}}^{1/2}(f)\right| \quad (13)$$

$$\left|Y_{TS2} - \text{[illegible]}\right| = \left|S_{TS_2}^{1/2}(f)/S_{\text{[illegible]}}^{1/2}(f)\right| \quad (14)$$

$$\left|Y_{\text{[illegible]}} - \text{[illegible]}\right| = \left|S_{\text{[illegible]}}^{1/2}(f)/S_{\text{[illegible]}}^{1/2}(f)\right| \quad (15)$$

Table 2. Mesh parameters during the optimization process.

Number of elements	Mesh type	Maximum element size (mm)	Minimum element size (mm)	Maximum element growth rate	Curvature factor	Resolution of narrow region
Highly refined	Free tetrahedral mesh	21.1	0.903	1.35	0.30	0.85

2.2. Thermoelastic optimization framework

The essence of the thermoelastic optimization is to replace manual selection with the optimization algorithms.The designs that better meet the objectives are iteratively identified, while the underlying physical principles are revealed. Thermoelastic optimization mainly consists of three blocks: parametric geometric modeling, thermoelastic simulation, and optimization algorithms. Fig. 4 shows the optimization framework, and the specific steps are as follow:

Step 1: The lengths of the supporting stage L_1 and the compensation stage L_2 are selected as the optimization variables as shown in Fig. 5 (a). Determine the number of optimization iteration m and the initial design parameters L_{10} and L_{20}.

Step 2: Construct the parametric geometric model of the object and then apply the design parameters.

Step 3: Import the geometric model into the CFD solver to perform the numerical simulations and obtain the result *Y*. Real-time transfer of the geometric model to the CFD solver can be achieved using Livelink for SolidWorks.

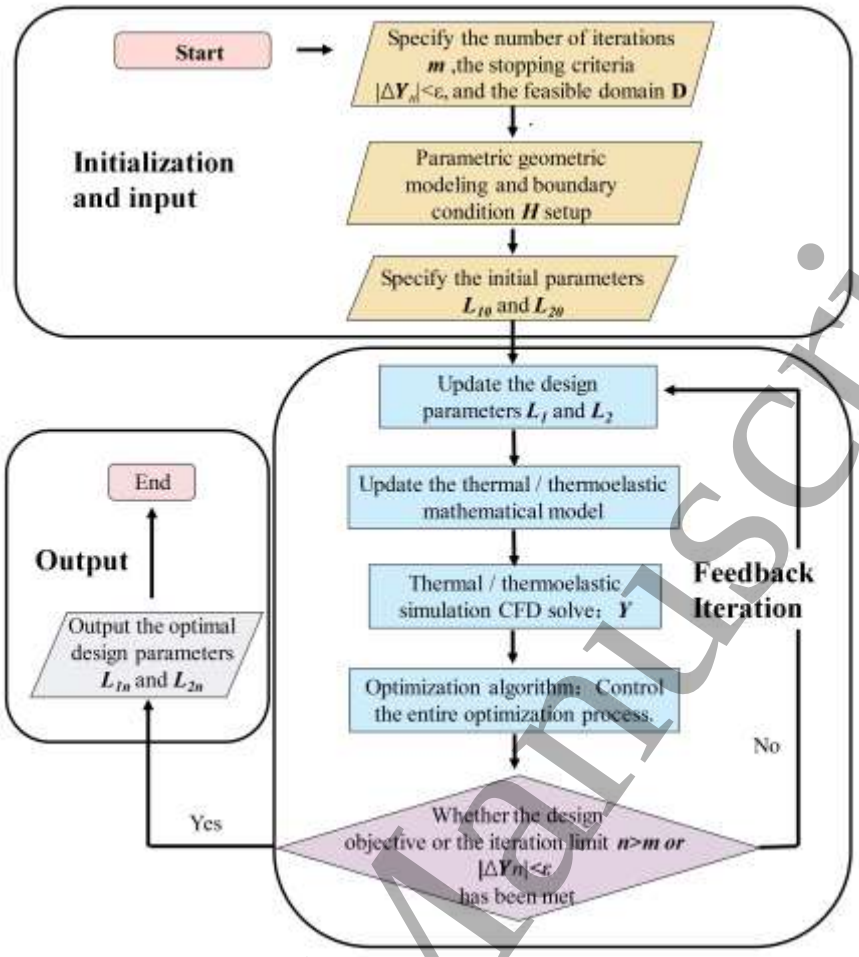

Figure 4. Schematic of the thermoelastic optimization framework.

Step 4: Feed the thermal simulation results into the optimization algorithm for further evaluations. The algorithm first checks whether the current design meets the design objectives or whether the maximum number of the iterations has been reached. If so, proceed to the next step; otherwise, the next optimization direction is determined based on the current results and the historical simulation data. The design parameters are updated, passed to the parametric geometry model, and the process returns to Step 3. Details of the optimization algorithm employed in this work are provided in the Appendix.

Step 5: Output the optimized design and terminate the iterative loop.

For the optimization problem, it is necessary to define appropriate boundary conditions. As described above, temperature noise is transmitted to the vacuum chamber through the ISS and subsequently affects the TM via internal heat transfer within the IS. Therefore, the constraints of the thermoelastic optimization problem should first be defined by the thermal attenuation problem. Fig. 5 (b) shows the TF corresponding to the different combinations of the random L_1 and L_2. Considering the spatial constraints within the payload compartment, the feasible domain D is defined $D = \{L \hat{I} \; ¡ \; |0 £ \; L < 500\text{mm}\}$. The TFs at TS_1 and TS_2 display random variability across different random combinations, remaining within an approximate range of $7 \times 10^{-6} \sim 2$

× 10^{-4} K/W for the selected range. Compared with TS_1, an additional temperature attenuation path is included to TS_2 and therefore $|Y_{TS2\text{-}\dot{P}\dot{P}}| < |Y_{TS1\text{-}\dot{P}\dot{P}}|$. Nevertheless, this difference remains below 10 % across all 20 combinations. Due to the high thermal diffusivity of the aluminum alloy, the temperature attenuation at TS_1 and TS_2 is close, and the magnitude of the temperature attenuation is primarily determined by the length L_1.

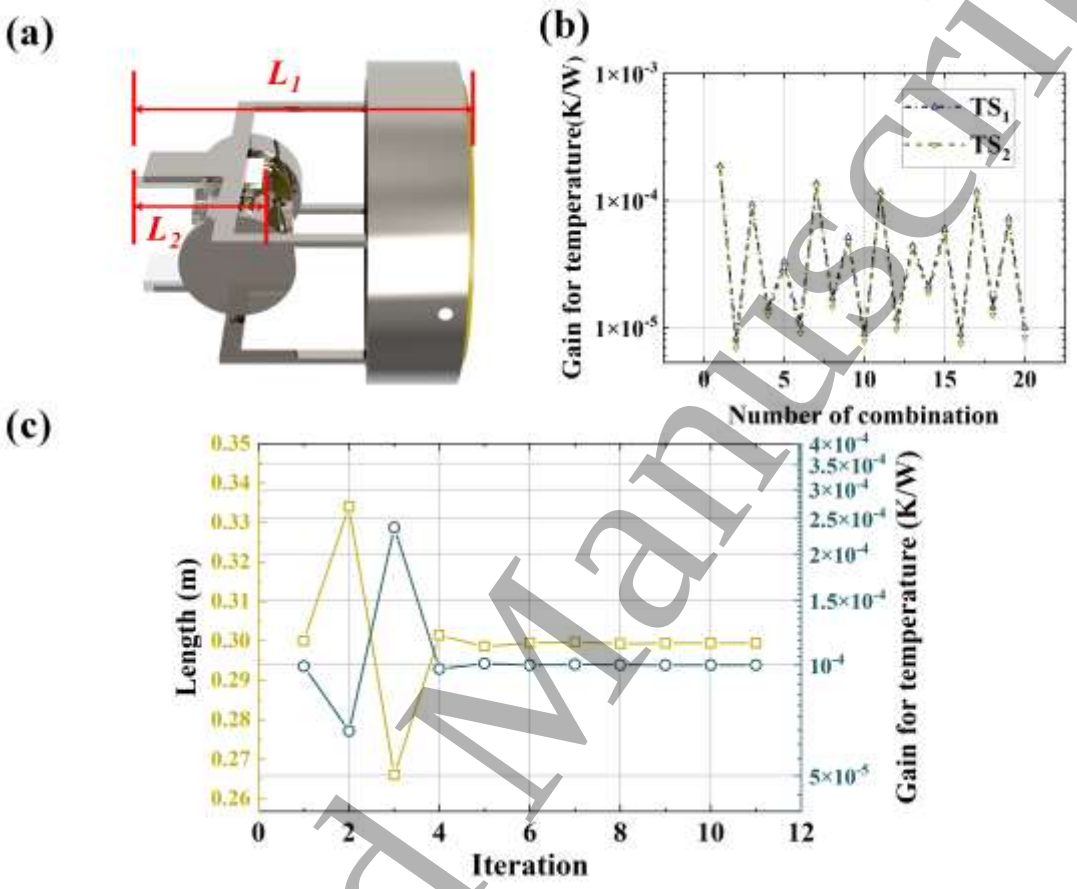

Figure 5. Determination of the optimization boundary conditions: (a) variables of optimization; (b) TF values under different random variable combination; (c) temperature-oriented thermal optimization results.

Previous studies have shown that the internal heat path of the IS provides a temperature attenuation capability of approximately 10^{-3} K/K [27]. Accordingly, the thermal requirement of L_1 can be solved using a thermal optimization approach to obtain the minimum value. To meet the temperature requirement of 5 μK/$Hz^{1/2}$, $|Y_{TS2\text{-}\dot{P}\dot{P}}(L_1)|$ is required to be below 10^{-4} K/W.

Fig. 5 (c) shows the results of the temperature-oriented thermal optimization. As the iterations proceed, the length of L_1 eventually stabilizes at approximately 300 mm. Accordingly, the constraints of the thermoelastic optimization problem to be solved in this study can be defined as $300mm \leq L_1 \leq 500mm$ and $30mm \leq L_2 \leq 250mm$.

3. Results and discussion

3.1 Sensitivity analysis

Optimization results are obtained using three different optimization algorithms, namely the Efficient Global Optimization (EGO) algorithm [33], the Nelder–Mead (NM) algorithm [34], and the Bound Optimization BY Quadratic Approximation (BOBYQA) algorithm [35]. Fig. 6 illustrates the iterative optimization processes of the different optimization algorithms at 0.1mHz. The initial identical design parameters L_{10} and L_{20} are specified as 300 mm and 180 mm according to the preliminary design of the support structure for both NM and the BOBYQA. Fig. 6 (a) compares the optimized lengths from different algorithms. BOBYQA and NM rapidly converge after the initial search, whereas EGO continues the global exploration. Fig. 6 (b) shows the gain for TED from different optimization algorithms. As the iterative process proceeds, the gain for TED decreases continuously for all three algorithms.

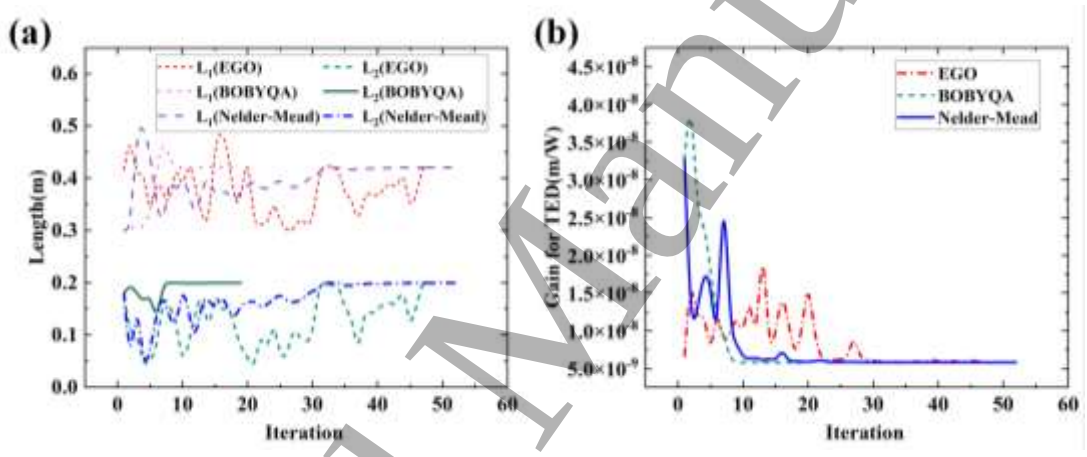

Figure 6. Comparison of the optimization processes using different algorithms at 0.1mHz: (a) optimized length obtained using different optimization algorithms; (b) TED gain of different optimization algorithms.

Table 3 provides a further comparison of the optimization results from the different algorithms. The obtained L_1 and L_2 and the TED gain are nearly identical, with the differences of less than 1% for all three methods. Specifically, L_{1av} is 0.4206 m and L_{2av} is 0.1999 m. These results indicate that the thermoelastic optimization problem is mathematically convex over the feasible domain, with no non-global local optima under the current thermal assumptions. By contrast, EGO requires the most simulations, about twice those of NM and five times those of BOBYQA. Given a runtime of ~15 min per thermoelastic simulation (CPU: 2 × EPYC 7742, memory: 128 GB, storage: 8 TB), BOBYQA substantially reduces the computational cost and is therefore adopted for the subsequent analyses. Notably, for EGO the iteration number does not equal the number of simulations and is typically larger, as the additional evaluations are required to construct the surrogate model before optimization.

Table 3. The impact of different optimization algorithms on the optimization results.

Optimization method	L_1 (m)	L_2 (m)	Gain for TED (m/W)	Number of evaluations
EGO	0.4203	0.2000	5.81×10^{-9}	96
Nelder-Mead	0.4207	0.1998	5.80×10^{-9}	53
BOBYQA	0.4208	0.2000	5.81×10^{-9}	19

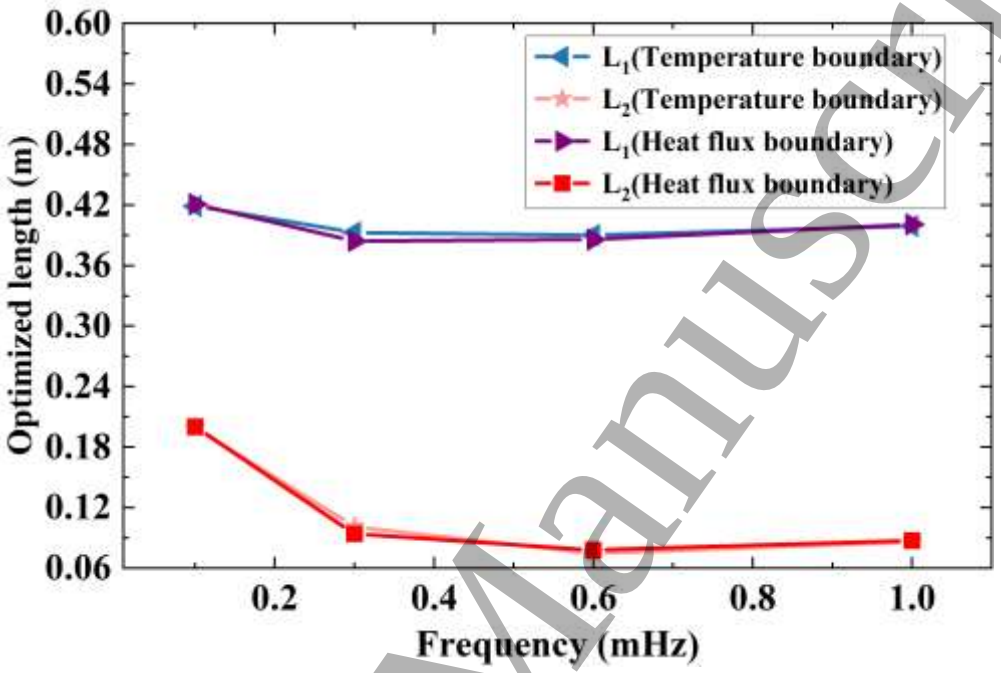

Figure 7. Comparison of the optimization results under different boundary conditions and frequencies.

Fig. 7 presents the optimization results under different boundary conditions and frequencies. At the same frequency, the optimization results exhibit deviations not exceeding 1 %, indicating that the optimized results are insensitive to the type of the boundary conditions. Accordingly, subsequent discussions focus solely under the heat flux boundary conditions. In contrast, the optimization results differ significantly across different frequencies. This will be discussed in detail in the subsequent sections.

In the process of model setup, several sources of uncertainty remain, such as the radiative effects of MLI and the influence of the contact heat transfer. Based on the equilibrium temperature T_0 of 283.15 ~ 303.15 K, and the equivalent surface emissivity of MLI of 0.02 ~ 0.06, the calculated effective radiative thermal resistance R_r ranges from 853 ~ 2573 K/W. By incorporating the estimated parameter ranges into the simulation, together with ray-tracing for thermal radiation and heat conduction modeling, updated optimization results are obtained, as summarized in Table 4. The obtained results show L_1 ranging from $0.4206^{+0.0002}_{-0.0028}$ m, while L_2 is between $0.1999^{+0.0001}_{-0.0014}$ m.

As for the influence of the thermal contact, due to the atomic-level metallurgical bonding, the friction-welded interface exhibits a superior thermal contact coefficient and negligible. For the bolted Al–Ti interface, two extreme cases are considered: an uninsulated case with direct screw connection[36], and an insulated case with a thermal insulation pad between the two layers. Consequently, the comprehensive range for the thermal contact coefficient h_c is 158 ~ 23100 W/(m^2·K). Taking the thermal contact coefficient into account, the optimized results for L_1 is $0.4206^{+0.0009}_{-0.0026}$ m and L_2 are obtained as $0.1999^{+0.0001}_{-0.0019}$ m. It is worth noting that, within the current thermal environment design of MOSA, the impacts of radiative and contact heat transfer on the ISS optimization results are each below 1%. The findings indicate that the optimization results are relatively insensitive to model uncertainties.

Furthermore, by incorporating the ranges of the thermal contact coefficient h_c and radiative thermal resistance R_r identified above into the 3D simulations of the optimized configuration, the TED performance is evaluated across the full frequency range. The result shows that the TED variation remains below 0.1%, indicating that the proposed geometry exhibits a certain degree of robustness to long-term drift without compromising thermoelastic performance.

Table 4. Impact of uncertainties in the heat transfer process on the optimization results

Source of uncertainty	Magnitude	L_1 (m)	L_2 (m)	Gain for TED (m/W)
Effective thermal radiation resistance (estimated values, not directly incorporated into simulation) R_r (K/W)	853	0.4178	0.1985	5.82×10^{-9}
	1500	0.4195	0.1999	5.81×10^{-9}
	2573	0.4208	0.2000	5.80×10^{-9}
Equivalent interface thermal contact coefficient h_c (W/(m^2·K))	158	0.4180	0.1980	5.80×10^{-9}
	5000	0.4192	0.1998	5.81×10^{-9}
	21300	0.4215	0.2000	5.81×10^{-9}

3.2 Frequency dependence of the optimization process

Owing to the linear relationship between the thermoelastic response and temperature as stated in Eq. 9 , the gain for TED also exhibits low-pass filter behavior consistent with the temperature transfer function. Fig. 8 illustrates the thermoelastic optimization process at different frequencies. As shown in Fig. 8 (a) and Fig. 8 (b), the overall trends of the search processes are highly similar, especially in the evolution of L_1 and TED for 0.1mHz and 0.3mHz. Nevertheless, the TED varies more at 0.1 mHz compared with 0.3 mHz, indicating a broader exploring space under identical boundary conditions. At 0.6 and 1 mHz, optimization variability is markedly reduced, with the TED search range shrinking to ~ 20 % and the optimization improvement is less significant than that at low frequencies.

As the frequency increases, TFs attenuate more rapidly along the structure per unit length, resulting in a very low level of TF at the compensation stage and ability to conpensate. Detailed numerical comparisons are provided in Fig. 9. At higher frequencies, the effect of the thermoelastic optimization becomes less evident. Restricting the constraint to 100 mm < L_1 < 300 mm, and the searching range for high frequency becomes broader. These solutions are not further discussed as they violate practical GW detection temperature noise constraints.

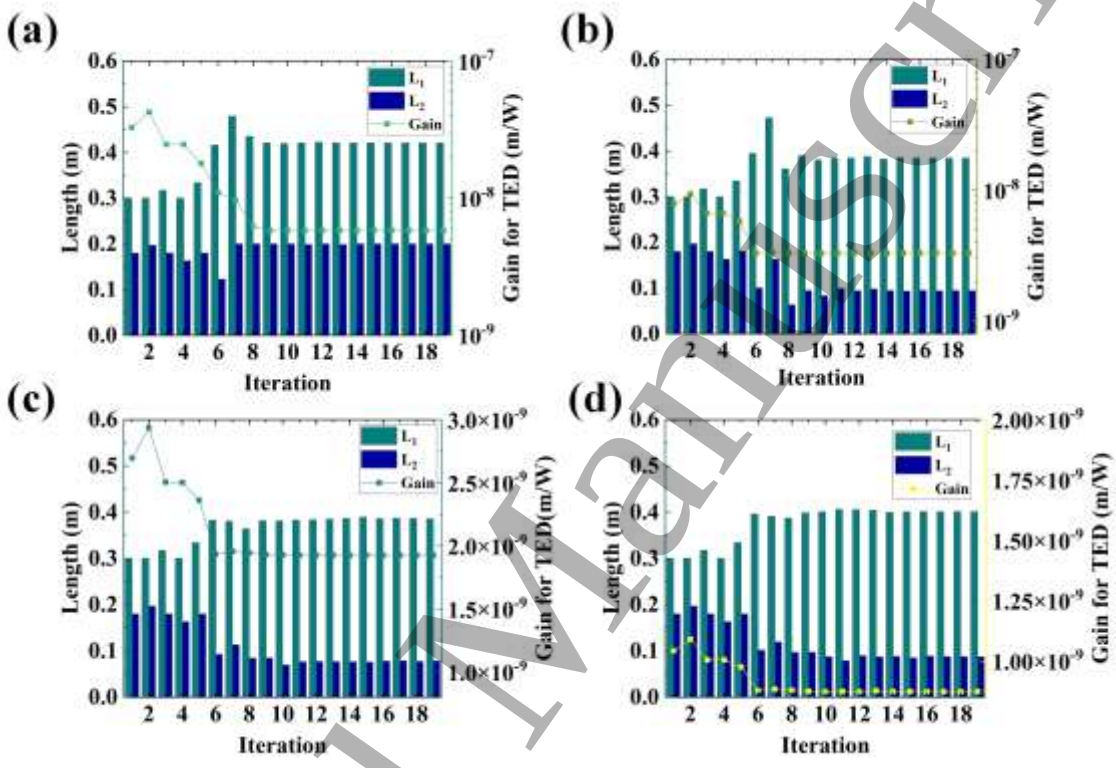

Figure 8. Comparison of thermoelastic optimization processes at different frequencies: (a) 0.1mHz; (b) 0.3mHz; (c) 0.6mHz; (d) 1mHz

3.3 Comparation before and after optimization

Fig. 9. illustrates the evaluation of the temperature noise before and after optimization. Temperature contour maps at 0.1mHz and 1mHz are shown in Fig. 9 (a-d). Temperature noise attenuates sequentially along the heat transfer path, propagating from the OB through the supporting stage and the compensation stage, and subsequently transmitting from the central region of the IS toward both sides and the interior. The optimization results in an extension of the lengths of both L_1 and L_2.

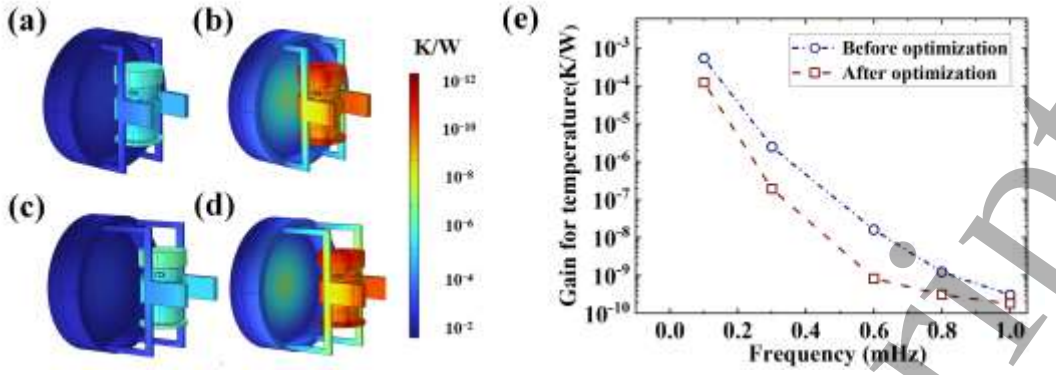

Figure 9. Comparison of the temperature noise before and after optimization: (a-b) temperature gain contours at 0.1mHz and 1mHz before optimization; (c-d) temperature gain contours at 0.1mHz and 1mHz after optimization; (e) temperature gain at TS_2

Fig. 9 (e) illustrates the evaluation of the temperature noise at TS_2 before and after optimization. Temperature gain at this point decreases from 6.44×10^{-4} K/W @ 0.1 mHz. to 0.94×10^{-4} K/W @ 0.1 mHz after optimization with extended L_1 and L_2. Due to the low-pass filtering characteristic of the temperature noise, the temperatures at all points above 0.1 mHz also decrease after optimization, resulting in an overall downward shift of the curve. The optimized results fully satisfy the constraint requirement that the gain be less than 10^{-4} K/W @ $f \geq 0.1$ mHz.

Following the analysis in Section 3.2, the optimization improvement is more significant at low frequencies, and the improve result at 0.1 mHz can be taken as the full-band optimum structure (FBOS). To further justify this point, optimization is performed within the bandwidth (0.1 mHz ~ 1 mHz). Fig. 10 (a) illustrates the comparison between other representative frequency and FBOS. When optimized structures are obtained at other frequencies (0.3, 0.6 and 1 mHz), the resulting curve still exhibits a low-pass filtering characteristic. However, since these structures are not optimized for 0.1 mHz (nor across other frequencies), the overall curve shows an upward shift, with a more pronounced increase at the lowest frequencies, where the values exceed those at 0.1 mHz. This observation holds when we compute and compare the optimized values at 0.5, 0.8 mHz and other frequency points. Therefore when the TED within the bandwidth is adopted as the objective function, , 0.1 mHz is the worst-case and the resulting optimized structure remains consistent with that obtained at the lowest frequency. Fig. 10 (b) further illustrates the comparison between the FBOS and the optimized solutions at each individual frequency. The optimized TED at other frequency points is reduced compared with FBOS. Nevertheless, this difference becomes less significant as the frequency increases and the difference is only 5.1 % at 1 mHz. Therefore, the loss in optimization effectiveness is acceptable when the lowest frequency optimized solution is used to represent the FBOS.

Fig. 10 (c) illustrates the frequency dependent gain for the TED at TS_2 for the FBOS. Within the considering frequency range, an overall downward shift of the curve is also observed, and the effect becoming especially evident at low frequencies. Specifically, the gain for the TED decreases from 3.28×10^{-8} m/W to 5.81×10^{-9} m/W@ 0.1 mHz. To isolate the contribution arising specifically from TED, it is assumed that no additional TED occurs elsewhere along the optical path. Under this assumption, the direct thermal dissipation on the OB is taken to be 3×0.85 mW/Hz$^{1/2}$[28]. Thermoelastic simulations indicate that the transfer function from the OB heat load to the relative displacement between OB and IS is approximately 2.45×10^{-10} m/W according to extension simulation results. Therefore, the equivalent displacement noise directly coupled into the interferometer readout is estimated to be approximately 0.06 pm/Hz$^{1/2}$. According to the interferometer noise budget of the TianQin mission, this contribution is required to be below 0.5 pm/Hz$^{1/2}$[4]. Therefore, the thermally induced OB–IS relative displacement predicted for the optimized structure is found to remain well below the allocated noise budget, indicating that the preliminary thermal stability requirements are satisfied by the current optimized structural design.

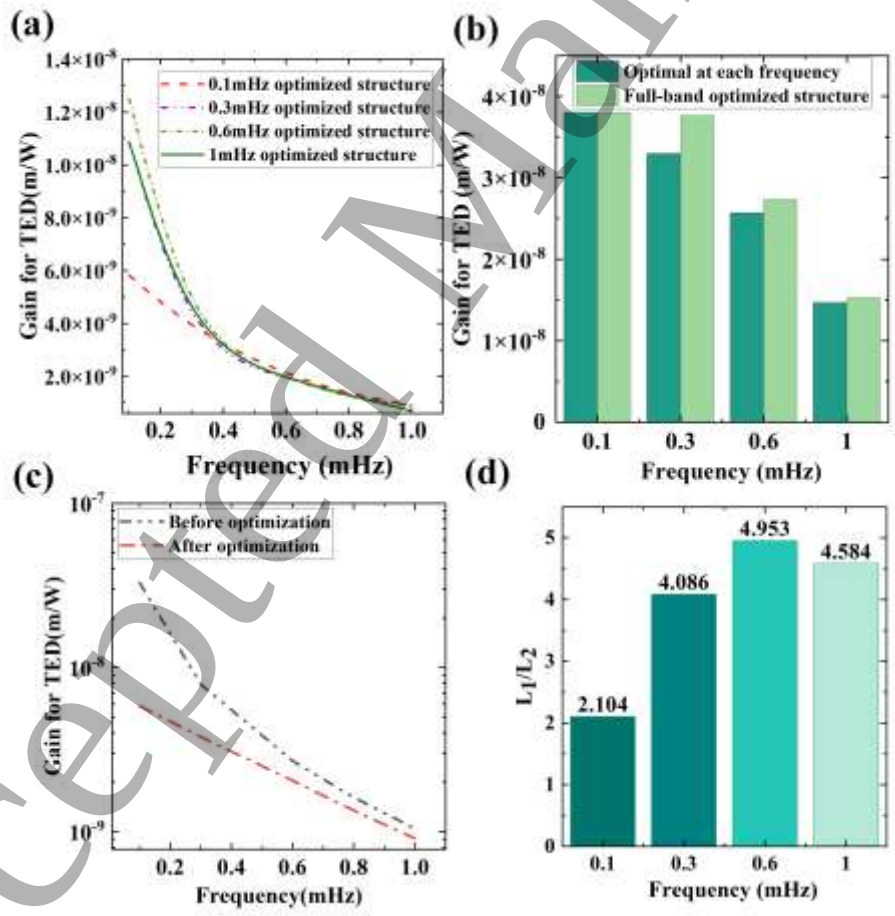

Figure 10. Frequency dependence of the TED before and after optimization: (a) comparison between representative frequency optimized and the full-band optimized structure at (0.1 mHz ~ 1 mHz); (b) comparison between frequency optimized and the full-band optimized structure

at representative frequency; (c) gain for TED at the end of the compensation stage; (d) frequency dependence of L_1/L_2.

In the case of an ideal one-dimensional TECS subjected to uniform temperature increase, the length is required to scale inversely with the CTE ratio α_2/α_1 in the time domain as shown in Eq. 16. When extended to the FD and realistic structures, it can be expected that the ratio is still related to α_2/α_1. Fig. 10 (c) presents the L_1/L_2 analysis at different frequencies. This ratio increases with frequency but shows a non-monotonic behavior. This is because that unlike one-dimensional thermoelastic structures, the present design includes an intermediate z-direction heat transfer stage that conducts heat but contributes negligibly to x-direction TED. The ratio of the length of non 1D heat transfer stage to that of the 1D heat transfer stage is defined as δ. By introducing δ, Eq. (17) is modified accordingly.

$$L_1(\mathrm{D}T_1)/L_2(\mathrm{D}T_2)\ \mu\ a_2/a_1 \tag{16}$$

$$L_1(\mathrm{D}T_1,f)/L_2(\mathrm{D}T_2,f)\sim a_2/a_1 d\cot(f) \tag{17}$$

3.4 Optimization design under more stringent constraints

In the practical designs, the absolute distance between the OB and IS is usually fixed, as it is constrained by the limited tuning range of the laser power. This distance varies in the different GW detectors. The distance can be expressed as an additional constraint $L_1 - L_2 = \mathrm{D}L_0$ and incorporated into the optimization.

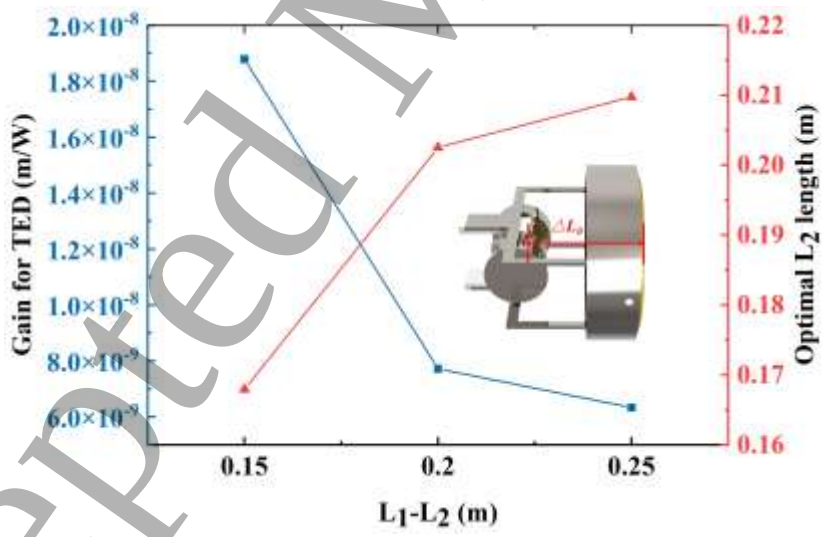

Figure 11. Optimization results under a prescribed temperature difference constraint at 0.1mHz (ΔL_0 = constant).

Fig. 11 presents the optimization results obtained under different ΔL_0 at 0.1 mHz. As ΔL_0 increases, the required length of L_2 increases accordingly. The length of L_1 also increases, leading to a reduction in the overall gain for TED. The resulting performance differs markedly from that obtained without additional constraints. The best achievable result is only $6.34 \times 10^{-}$

^{9} m/W @ 0.1 mHz and fails to reach the unconstrained optimum value of 5.81×10^{-9} m/W @ 0.1 mHz. This result indicates a certain loss in the optimization performance induced by the extra constraints.

Table 5 further compares the optimized ratios under varying ΔL_0. It can be observed that the obtained results deviate from the optimized ratio identified in the previous analysis. This deviation mainly arises from δ. As the overall length increases, the proportion of the intermediate structural segment that does not satisfy the one-dimensional thermoelastic assumption becomes smaller, and its influence becomes less pronounced. This is reflected in Table 5 as the smallest bias from the optimized ratio obtained without the extra constraint.

Table 5. Comparative analysis of optimized ratios under varying length differences

L_1-L_2(m)	L_1(m)	L_1/L_2	Bias %
0.15	0.318	1.893	10.0
0.20	0.413	1.941	7.7
0.25	0.460	2.192	4.2

The above discussion focuses on the single-direction optimization of the support and compensation stages. Based on the actual operating conditions of the TianQin project, a structural scheme more consistent with practical TianQin requirements is proposed, as shown in Fig. 12.

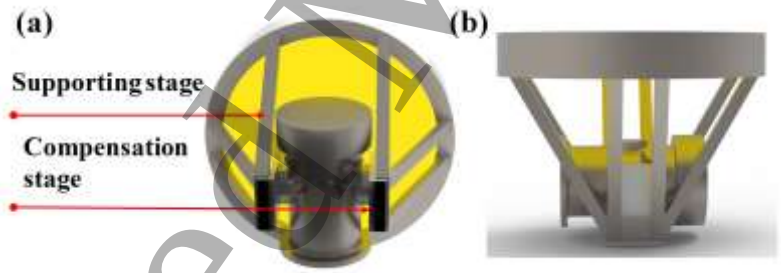

Figure 12. Structure diagram of the premilinary support structure design for the TianQin inertial sensor: (a) front view; (b) side view.

While maintaining the overall length consistent with the previous optimization conclusions, the preliminary design first improved the original orthogonal support into a diagonal bracing configuration to address its limitations. Furthermore, two stiffening ribs are introduced on the lateral sides. This composite design strategy specifically reinforces the lateral mechanical performance, significantly enhancing the lateral stiffness and the disturbance resistance, thereby yielding an optimized structure that is more practical for the engineering implementation. Building upon this preliminary structure, the TianQin team is conducting iterative design on the support systems of the TianQin inertial sensor. It is important to note that practical engineering applications involve real-world variables and have influence on the

practical optimal optimization results and the long term TED of the structure. Consequently, the theoretical optimized values must be further refined and validated through ground-based experiment. The TianQin team is expected to conduct subsequent experimental studies.

4. Conclusion

Optimization design strategy for TED compensation structures in the GW detection is proposed, with coupling effects derived from the FD thermoelastic simulations in this work. A coupled TED optimization framework is established, integrating parametric geometry, thermoelastic simulation, and optimization algorithms, and three algorithms—EGO, BOBYQA, and NM—are employed and compared. The sensitivity of the optimization process, its FD dependence, the comparison of results before and after optimization, and the results under more stringent constraints are analyzed in this work. The main conclusions are as follows:

The steady heat source Q_0 or the steady temperature boundary T_0 are almost not coupled to the harmonic component of the TED response. Moreover, the optimization problem under the current thermal assumptions can be classified as a convex optimization problem. The optimization results exhibit no significant dependence on the type of the boundary conditions and the uncertainties of the TE model. In addition, the optimized solution obtained at the lowest frequency within the bandwidth can be used as that over the entire frequency band. After optimization, the temperature noise is reduced to 0.94×10^{-4} K/W @ 0.1 mHz, which is below the prescribed requirement. Meanwhile, the gain for TED decreases from 3.28×10^{-8} m/W @ 0.1 mHz to 5.81×10^{-9} m/W @ 0.1 mHz. In contrast to the relationship with the CTE in the time domain, L_1/L_2 exhibits a pronounced frequency dependence in the FD. Furthermore, the introduction of more stringent constraints leads to a certain degradation in the optimized performance.

The optimization strategy proposed in this work can be applied to a broader range of structural designs for the GW detectors. For problems in which the parametric modeling is allowed and the FD simulation results can be formulated as the optimization variables, the workflow proposed in this work enables automated optimization and significantly improves design efficiency.

Acknowledgements

We would like to thank the National Key R&D Program of China (Grant Numbers 2024YFC2207001) for its financial support.

Appendix

In this study, three optimization algorithms are employed, in sequence the EGO algorithm, the NM algorithm, and the BOBYQA algorithm.

EGO is a powerful global optimization algorithm specifically developed for expensive black-box functions. The number of the function evaluations is severely constrained by the computational time or cost. The method is grounded in Response Surface Methodology and employs a stochastic process surrogate model, commonly referred to as the DACE (Design and Analysis of Computer Experiments) or Kriging model. Figure A13 shows a schematic flowchart of the EGO algorithm.

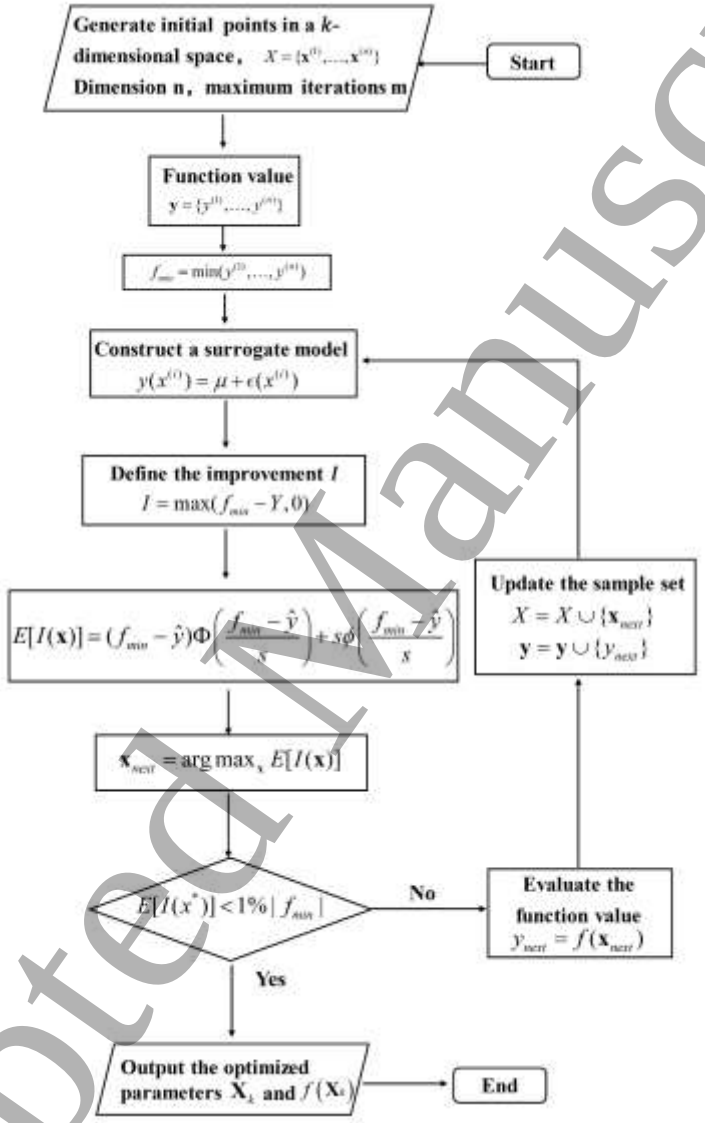

Figure A13. Schematic flowchart of the EGO algorithm

The NM algorithm, also known as the downhill simplex method, is a robust derivative-free optimization technique for identifying local minima in the multidimensional parameter spaces. Unlike gradient-based methods, it operates without explicit derivative information and instead employs a geometric simplex composed of n+1 vertices in an n-dimensional space. The simplex evolves through reflection, expansion, and contraction operations in response to the underlying

function landscape. In physics applications, this method is particularly valuable for optimizing black-box functions or handling noisy experimental data, where reliable gradient evaluation is computationally infeasible or physically impractical. Figure A13 shows a schematic flowchart of the NM algorithm.

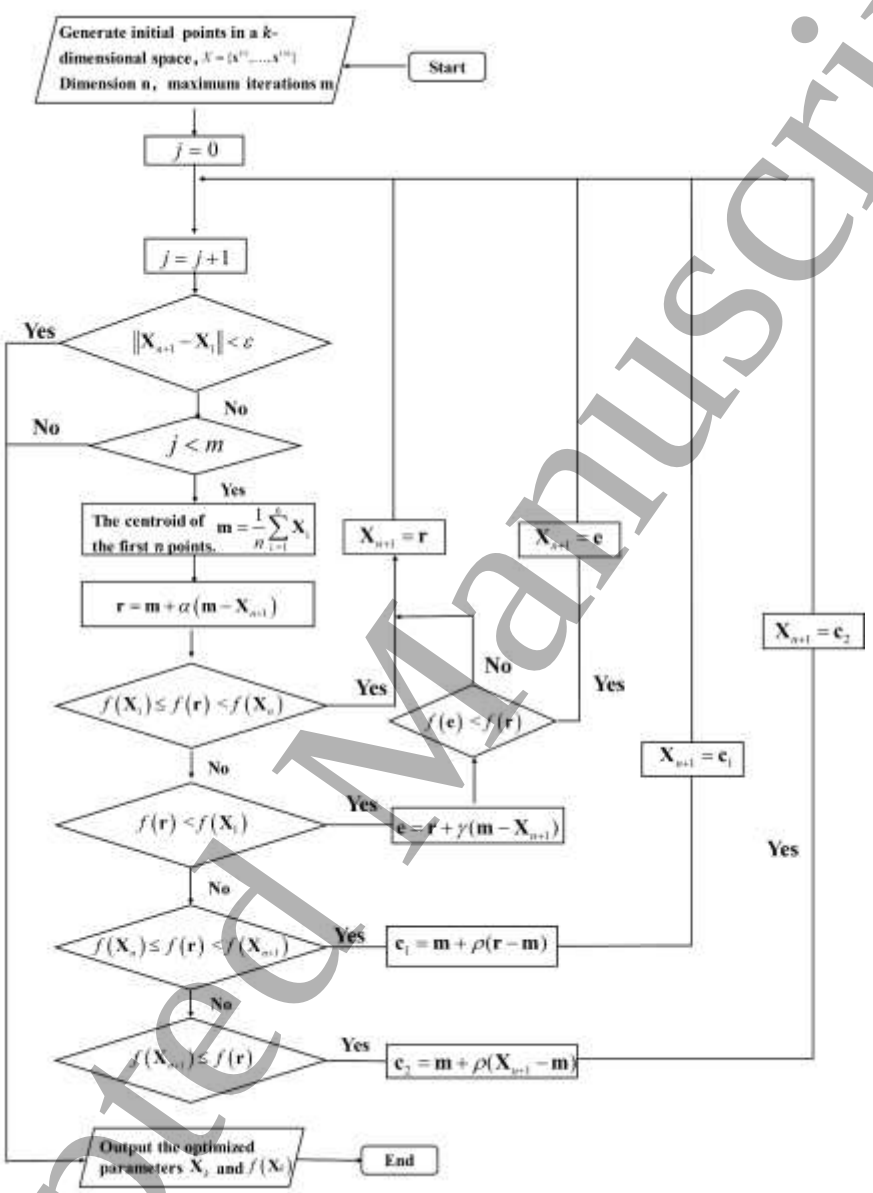

Figure A14. Schematic flowchart of the NM algorithm

The BOBYQA algorithm is a highly efficient, derivative-free numerical optimization method developed by M.J.D. Powell for solving non-linear problems with bound constraints. As illustrated in Figure A14, the algorithm operates by iteratively constructing a quadratic model Q(x) that interpolates a set of points Y within a predefined trust region. The algorithm solves a subproblem to find a trial point X_{trial} within this trust region defined by the radius Δ_k that promises the greatest reduction in the objective function. It then evaluates the ratio r between

the actual reduction in the function value ρ_{actual} and the predicted reduction from the model ρ_{text} to decide whether to expand or contract the trust region radius. This approach makes it exceptionally suitable for complex engineering simulations where the objective function is expensive to calculate, lacks an analytical gradient, or is subject to strict parameter limits.

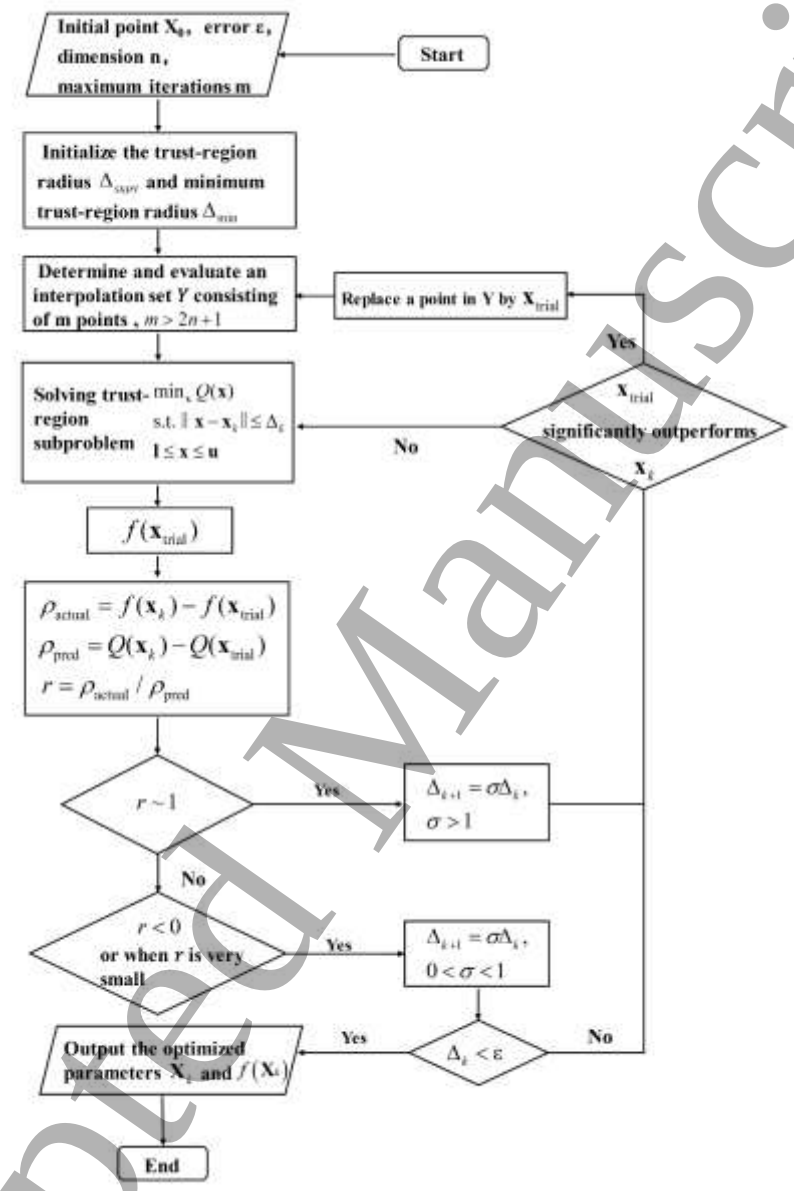

Figure A15. Schematic flowchart of the BOBYQA algorithm

References

[1] J. Luo, S. Bai, Y. Bai,et.al, Progress of the TianQin project, Class. Quantum Gravity 42 (17) (2025) 173001. https://doi.org/10.1088/1361-6382/adda8a.

[2] Y. Hu, J. Mei, J. Luo, Science prospects for space-borne gravitational-wave missions, Natl. Sci. Rev. 4 (5) (2017) 683-684. https://doi.org/10.1093/nsr/nwx115.

[3] K. Danzmann, T.L.S. Team, LISA: laser interferometer space antenna for gravitational wave measurements, Class. Quantum Gravity 13 (11A) (1996) A247-A250.

https://doi.org/10.1088/0264-9381/13/11A/033.

[4] J. Luo, L. Chen, H. Duan,et.al, TianQin: a space-borne gravitational wave detector, Class. Quantum Gravity 33 (3) (2015) 35010-35028. https://doi.org/10.1088/0264-9381/33/3/035010.

[5] J. Luo, Y. Bai, L. Cai,et.al, The first round result from the TianQin-1 satellite, Class. Quantum Gravity 37 (18) (2020) 185013. https://doi.org/10.1088/1361-6382/aba66a.

[6] H. Chen, C. Ling, X. Zhang,et.al, Thermal environment analysis for TianQin, Class. Quantum Gravity 38 (15) (2021) 155015. https://doi.org/10.1088/1361-6382/ac0a85.

[7] G. Li, J. Ke, H. Li,et.al, Thermal induced noise on test mass with copper alloy electrode housing for spaceborne gravitational wave detection, Phys. Rev. D 109 (8) (2024). https://doi.org/10.1103/physrevd.109.082001.

[8] F.R. Garcia, Thermo-optical and thermo-elastic effects onboard the LISA pathfinder mission, in, Ph.D dissertation, 2019.

[9] W. Chang, Y. Wang, W. Tan,et.al, Earth–lunar thermal effect on the temperature stability of TianQin telescope and the suppression methods, Case Stud. Therm. Eng. 67 (2025) 105816. https://doi.org/10.1016/j.csite.2025.105816.

[10] F. Gibert, M. Nofrarias, N. Karnesis,et.al, Thermo-elastic induced phase noise in the LISA pathfinder spacecraft, Class. Quantum Gravity 32 (4) (2015) 45014. https://doi.org/10.1088/0264-9381/32/4/045014.

[11] D. Wang, X. Zhang, L. Zhang,et.al, Long-term thermal stability of TianQin satellites, Phys. Rev. D 109 (10) (2024) 102007. https://doi.org/10.1103/PhysRevD.109.102007.

[12] Y. Liu, Z. Zhou, Progress in the development of space inertial sensor for TianQin project, Int. J. Mod. Phys. D (2024) 2540007. https://doi.org/10.1142/S0218271825400073.

[13] H.J. Juranek, G. Kleer, W. Doell, Use of glass ceramic as a structural material for a high-precision space telescope, in: Space Optics '94, SPIE, 1994, pp. 407-418. https://doi.org/https://doi.org/10.1117/12.188101.

[14] N.C. Jessen, H.U. Norgaard-Nielsen, J. Schroll, Carbon fibre reinforced plastic structures for instruments for very large and extremely large telescopes, in: Optics and Photonics 2005, SPIE, 2005, pp. 213-224. https://doi.org/https://doi.org/10.1117/12.614859.

[15] J. Sanjuan, A. Preston, D. Korytov,et.al, Carbon fiber reinforced polymer dimensional stability investigations for use on the laser interferometer space antenna mission telescope, Rev. Sci. Instrum. 82 (12) (2011). https://doi.org/https://doi.org/10.1063/1.3662470.

[16] C.R. Sandin, L.N. Allen, E.G. Amatucci,et.al, Materials evaluation for the origins space telescope, J. Astron. Telesc. Instrum. Syst. 7 (1) (2021) 11011. https://doi.org/https://doi.org/10.1117/1.JATIS.7.1.011011.

[17] P. Hartmann, R. Jedamzik, A. Carré,et.al, Glass ceramic ZERODUR®: even closer to zero thermal expansion: a review, part 1, J. Astron. Telesc. Instrum. Syst. 7 (2) (2021) 20901. https://doi.org/https://doi.org/10.1117/1.JATIS.7.2.020901.

[18] S. Lucarelli, D. Scheulen, D. Kemper,et.al, The breadboard model of the LISA telescope assembly, in: International Conference on Space Optics, SPIE, 2017, pp. 161-167. https://doi.org/https://doi.org/10.1117/12.2309050.

[19] L. Yang, L. Wei, L. Zhang, Thermal compensation design of truss structure for large-scale off-axis three-mirror space telescope, Opt. Eng. 58 (02) (2019) 1. https://doi.org/10.1117/1.oe.58.2.023109.

[20] J. Pijnenburg, M. Te Voert, J. de Vreugd,et.al, Ultra-stable isostatic bonded optical mount design for harsh environments, in: International Conference on Space Optics, SPIE, 2012, pp. 744-755. https://doi.org/https://doi.org/10.1117/12.2309082.

[21] J. Etchells, Thermo-elastic analysis in the frequency domain using the LISA instrument as a case study, in: 50th International Conference on Environmental Systems, 2021.

[22] C. Diekmann, Development of core elements for the LISA optical bench: electro-optical measurement systems and test devices, Ph.D dissertation, Leibniz Universität Hannover, 2013.

[23] E. Hailer, J. Burkhardt, M. Altenburg, Linear control analysis & review for systema – utilization of complex thermo-elastic transfer functions, in: 51st Intemnational Conference on Environmental Systems, 2022.

[24] B. Li, Y. Yan, J. Luo,et.al, Multi-optimization for thermal deformation of gravitational wave telescope based on CFRP characteristics, Sci. Rep. 14 (1) (2024) 14943. https://doi.org/10.1038/s41598-024-65836-1.

[25] Y. Diao, W. Tao, X. Deng,et.al, Non-magnetic negative coefficient of thermal expansion support structure between payloads in the taiji space gravitational wave detection satellite, Machines 11 (10) (2023) 948. https://doi.org/10.3390/machines11100948.

[26] J. Meseguer, I. Pérez-Grande, A. Sanz-Andrés, Spacecraft thermal control, Elsevier, 2012.

[27] F. Wei, X. Luo, S. Qu,et.al, Low frequency thermal stability of the TianQin inertial sensor, Int. Commun. Heat Mass Transf. 164 (2025) 108960. https://doi.org/10.1016/j.icheatmasstransfer.2025.108960.

[28] Y. Wang, W. Tan, W. Chang,et.al, Thermal-insulation design for low-frequency temperature stability of inertial sensors in the TianQin project through frequency-domain analysis, Phys. Rev. Appl. 24 (2) (2025) 24004. https://doi.org/10.1103/r47s-bhdg.

[29] Y. Wang, W. Tan, W. Chang,et.al, Thermal analysis of the inertial sensor during the preliminary stage of the TianQin project, Phys. Rev. Appl. 23 (3) (2025). https://doi.org/10.1103/PhysRevApplied.23.034056.

[30] C.M. Guide, Structural mechanics module user's guide, COMSOL AB (2008).

[31] M. Nofrarias, A.F.G. Marín, A. Lobo,et.al, Thermal diagnostic of the optical window on board LISA pathfinder, Class. Quantum Gravity 24 (20) (2007) 5103-5121. https://doi.org/10.1088/0264-9381/24/20/012.

[32] S. Appel, J. Wijer, Simulation of thermoelastic behaviour of spacecraft structures, Springer, 2022.

[33] D.R. Jones, M. Schonlau, W.J. Welch, Efficient global optimization of expensive black-box functions, J. Glob. Optim. 13 (4) (1998) 455-492. https://doi.org/10.1023/A:1008306431147.

[34] M.A. Luersen, R. Le Riche, F. Guyon, A constrained, globalized, and bounded nelder–mead method for engineering optimization, Struct. Multidiscip. Optim. 27 (1) (2004) 43-54. https://doi.org/10.1007/s00158-003-0320-9.

[35] M.J. Powell, The BOBYQA algorithm for bound constrained optimization without derivatives,

Cambridge NA Report NA2009/06, University of Cambridge, Cambridge 26 (2009) 26-46.

[36] V. Sartre, M. Lallemand, Enhancement of thermal contact conductance for electronic systems, Appl. Therm. Eng. 21 (2) (2001) 221-235. https://doi.org/10.1016/s1359-4311(00)00034-x.